

RHEINISCHE FRIEDRICH-WILHELMS-UNIVERSITÄT BONN

ADVANCED LABORATORY COURSE

PERFORMED ON: MARCH 16, 2022

E106: Cavities

Authors

Paarth Thakkar
Keito Watanabe

Head Tutor

Dr. Michael Switka

Contents

| | | |
|----------|---|-----------|
| 1 | Introduction | 2 |
| 2 | Theoretical Background | 3 |
| 2.1 | Waveguides | 3 |
| 2.1.1 | Cylindrical waveguides | 4 |
| 2.1.2 | Cylindrical waveguides resonator | 4 |
| 2.2 | Oscillating circuit | 5 |
| 2.2.1 | Quality factor | 6 |
| 2.2.2 | Coupling coefficient | 6 |
| 2.2.3 | Reflection coefficient | 6 |
| 2.2.4 | Shunt impedance | 7 |
| 2.3 | Scalar measurement of reflection coefficient | 7 |
| 2.4 | Vectorial measurement of reflection coefficient | 8 |
| 2.4.1 | Determining resonant frequency and coupling | 9 |
| 2.4.2 | Determining quality factor | 10 |
| 2.4.3 | Determining Power Loss | 10 |
| 2.5 | Bead pull measurement | 10 |
| 2.5.1 | Resonant bead pull measurement | 10 |
| 2.5.2 | Non-resonant bead pull measurement | 11 |
| 2.5.3 | Shunt impedance | 11 |
| 2.6 | dB and dBm | 11 |
| 3 | Exercise before the experiment | 13 |
| 4 | Setup and Procedure | 14 |
| 4.1 | Experimental Setup | 14 |
| 4.2 | Procedure | 15 |
| 4.2.1 | Attenuation and Reflection in Coaxial Cables | 15 |
| 4.2.2 | Scalar Measurement | 16 |
| 4.2.3 | Vectorial Measurement | 18 |
| 4.2.4 | Bead-Pull Measurement | 18 |
| 5 | Results and Discussion | 20 |
| 5.1 | Attenuation of Coaxial Cables | 20 |
| 5.2 | Scalar Measurement | 20 |
| 5.3 | Vectorial Measurement | 21 |
| 5.4 | Bead-Pull Measurement | 22 |
| 6 | Conclusion and Outlook | 24 |
| 6.1 | Conclusion | 24 |
| 6.2 | Outlook | 24 |
| 7 | Appendix | 25 |

Chapter 1

Introduction

In this experiment, we study the various characteristics of a cavity. These characteristics help quantify how good the cavity is. Before talking about cavities themselves though, it is important to understand why we are studying them. Cavity resonators are important optical and microwave system components [1]. The main principle is that it has constructive and destructive interference pattern inside and enclosed region. They can be used as a filters, or as antennas or in lasers. They also have a wide range of application in particle accelerators [2].

x In today's report, we will first discuss the theoretical background, which gives us an insight on the working of cavities and how it works. Then we move on to the experimental setup and procedure. We end with results from our analysis and discussion.

Chapter 2

Theoretical Background

2.1 Waveguides

In order to understand cavities, we start off with the discussion on waveguides. An electromagnetic wave, when confined to the interior of a hollow pipe is called a waveguide. We shall closely follow the laboratory script [3] for our report. The generalized Maxwell equations in terms of E-field and H-field are given by:

$$\nabla \times \mathbf{E} = -\frac{\partial \mathbf{B}}{\partial t} \quad (2.1.1)$$

$$\nabla \cdot \mathbf{D} = \rho \quad (2.1.2)$$

$$\nabla \times \mathbf{H} = \vec{j} + \frac{\partial \mathbf{D}}{\partial t} \quad (2.1.3)$$

$$\nabla \cdot \mathbf{B} = 0 \quad (2.1.4)$$

In vacuum, these equations become:

$$\nabla \times \mathbf{E} = \mu_0 \cdot \frac{\partial \mathbf{H}}{\partial t} \quad (2.1.5)$$

$$\nabla \cdot \mathbf{E} = 0 \quad (2.1.6)$$

$$\nabla \times \mathbf{H} = \epsilon_0 \cdot \frac{\partial \mathbf{E}}{\partial t} \quad (2.1.7)$$

$$\nabla \cdot \mathbf{H} = 0 \quad (2.1.8)$$

Upon solving these equations, we get plane wave solutions which looks like this:

$$\Delta \vec{E}(\vec{r}) + \frac{\omega}{c^2} \vec{E}(\vec{r}) = 0$$

$$\Delta \vec{B}(\vec{r}) + \frac{\omega}{c^2} \vec{B}(\vec{r}) = 0$$

Now, let us look at a waveguide which is aligned along the z-direction. Taking the ansatz $\vec{E} = \vec{E}(x, y) e^{i(\omega t - kz)}$ and the separation $\Delta = \Delta_{\perp} + \frac{\partial^2}{\partial z^2}$, for the longitudinal fields yields:

$$\Delta_{\perp} E_z + k_c^2 E_z = 0 \quad (2.1.9)$$

$$\Delta_{\perp} H_z + k_c^2 H_z = 0 \quad (2.1.10)$$

where

$$k_c^2 = \frac{\omega^2}{c^2} - k^2$$

The quantity k_c is called the critical wave number and is a characteristic property of the cavity, as we shall see. Solving these equations further, we see that it is sufficient to know the longitudinal fields, E_z and B_z because we can easily determine the transverse components from them.

$$ik_c^2 \vec{E}_{\perp} = k \vec{\nabla}_{\perp} E_z + \omega \mu_0 \vec{\nabla}_{\perp} H_z \times \hat{e}_z \quad (2.1.11)$$

$$ik_c^2 \vec{H}_{\perp} = k \vec{\nabla}_{\perp} H_z - \omega \epsilon_0 \vec{\nabla}_{\perp} E_z \times \hat{e}_z \quad (2.1.12)$$

Now, there are two waves to classify these waves:

1. $k_c^2 = 0$
 - (a) $\vec{\Delta}_\perp E_z \neq 0$ and $\vec{\Delta}_\perp H_z \neq 0$: HE or EH hybrid waves.
 - (b) $\vec{\Delta}_\perp E_z = 0$ and $\vec{\Delta}_\perp H_z = 0$: TEM waves.
2. $k_c^2 \neq 0$ In this case we do not get any propagation if $\omega \leq c \cdot k_c$. These waves are called evanescent waves or the cut off condition. The possible propagation modes are:
 - (a) $E_z = 0$: TE (transversal electric) or H waves.
 - (b) $H_z = 0$: TM (transversal magnetic) or E waves.

Corresponding to this critical wave, we have a critical frequency, which is $\omega_c = k_c \cdot c$, below which there is no propagation. One interesting thing to note here is that for a hollow waveguide, only TE or TM modes are possible, TEM is not, because no wave would exist in this case [4]. But for a coaxial cable, which consists of straight wire surrounded by a conduction sheath, we can get TEM modes.

2.1.1 Cylindrical waveguides

We now consider a cylindrical waveguide with an inner radius a . This imposes the following boundary conditions to the walls of the waveguide:

- $E_\phi = 0, E_z = 0$ for $r = a$
- $H_r = 0$ for $r = a$

The field distribution solution for a cylindrical waveguide can be separated into angular and radial parts, whose solutions are then given by the Bessel/Neumann functions. These can be then substituted in the eq.(2.1.11)-(2.1.12) and upon imposing the constraints from the boundary condition gives us the corresponding TE- and TM-modes.

2.1.2 Cylindrical waveguides resonator

The time has now come, to talk about cavities itself. If we now insert two conducting plates perpendicular to the z-axis, the incoming wave is reflected completely, giving us standing waves. Because of this, the z-dependence changes like:

$$a \cdot e^{ikz} \implies A \cdot \sin(kz + \phi_0)$$

The following condition is imposed so that the longitudinal boundary conditions are fulfilled: $k = p \cdot \pi/l$. The longitudinal field looks like:

$$\begin{aligned} \textbf{TE}_{mnp} - \textbf{Modes} : H_z &= H_{mn} \cdot J_m(k_c r) \cos(m\phi) \cdot \sin(p\pi/l \cdot z) \cdot e^{\omega_{mnp} t}; \\ &\text{where } k_c a = j'_{mn} \\ \textbf{TM}_{mnp} - \textbf{Modes} : E_z &= E_{mn} \cdot J'_m(k_c r) \cos(m\phi) \cdot \cos(p\pi/l \cdot z) \cdot e^{\omega_{mnp} t}; \\ &\text{where } k_c a = j_{mn} \end{aligned}$$

For resonant frequency, we have:

$$\omega_{mnp} = c \cdot \sqrt{(j_{mn}/a)^2 + (p\pi/l)^2}$$

Here, J_m is the m -th Bessel function, J'_m is its derivative. And j_{mn} and j'_{mn} are the n -th zeropoints of the m -th Bessel function and its derivative.

The resonant modes can be written in the linear form as:

$$(d\nu)^2 = \left(\frac{c j_{mn}^{(')}}{\pi} \right)^2 + \left(\frac{c}{2} \right)^2 p^2 \left(\frac{d}{l} \right)^2 \quad (2.1.13)$$

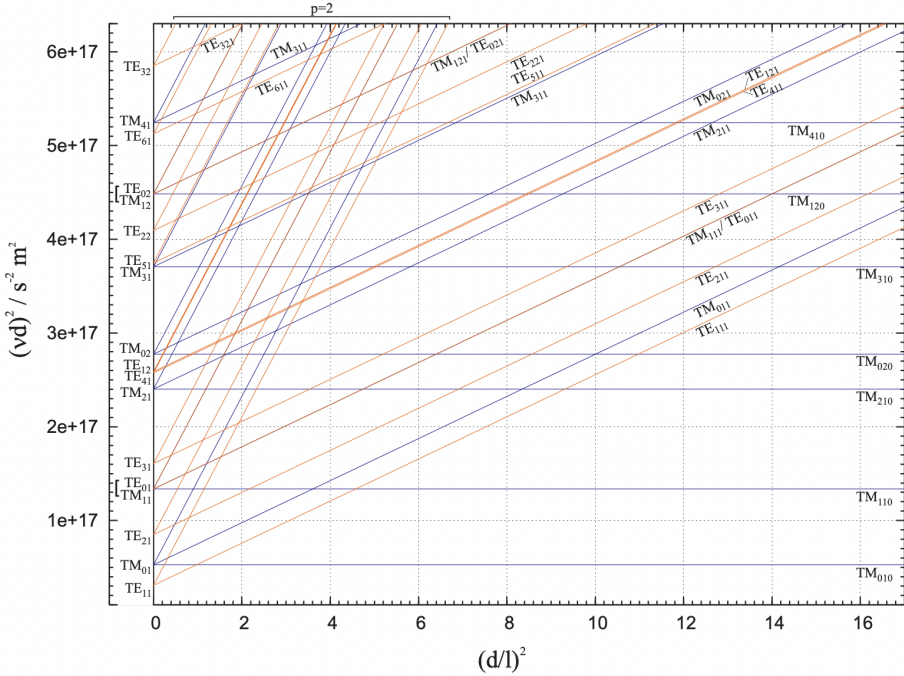


Figure 2.1.1: Mode map for $p \leq 2$. [3]

here d is the diameter of the cavity. When we plot different modes on a graph, we get a mode map (Fig.2.1.1). The mode map allows one to read off the resonant frequencies for different diameters and length of the cavity.

Since the derivative of the zeroth order Bessel function and the first order Bessel function, j_{0n}' and j_{1n} , are equal, the corresponding TE- and TM-modes have the same resonant frequencies. That is, TE_{0np} -modes and TM_{1np} -modes have the same resonant frequency.

In linear accelerators and accelerating resonators to accelerate ultra-relativistic particles, the TM_{01} mode is used.

2.2 Oscillating circuit

A cavity has a lot of characteristic quantities, which can be described by an equivalent circuit (Fig.2.2.1).

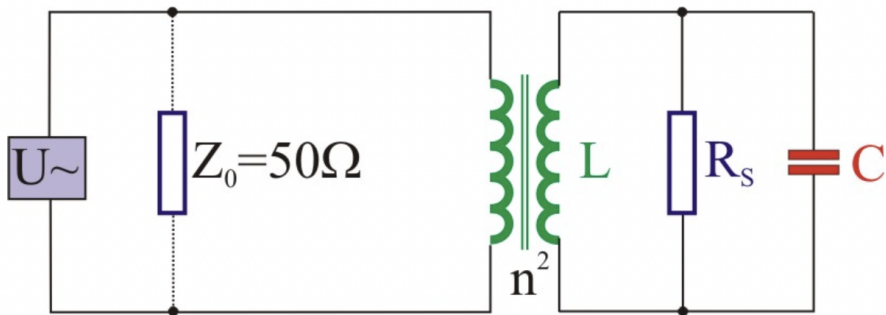


Figure 2.2.1: Equivalent circuit of a cavity with loop coupling. [3]

Coupling is a process through which electromagnetic waves can be coupled to a waveguide, or in this case, to a cavity. There are several ways to couple and in this experiment, we use loop coupling, which

enables coupling to the magnetic field inside the cavity. In the figure 2.2.1, the LCR-circuit represents the cavity. The step-down transformer represents the loop coupling, Z_0 is the characteristic impedance and R_s is the Shunt impedance.

The characteristic quantities associated with the cavity are:

- Quality factor
- Coupling coefficient
- Reflection coefficient
- Shunt impedance

Let us look at these quantities in a bit more detail.

2.2.1 Quality factor

Quality factor is a dimensionless quantity which describes how underdamped an oscillator or resonator is. It is defined as:

$$Q_0 = \frac{2 \cdot \pi \text{ stored energy}}{\text{losses per period}} = \frac{2\pi \cdot W}{T \cdot P} = \frac{\omega_0 \cdot W}{P} \quad (2.2.1)$$

where ω_0 is the angular resonant frequency. Looking at the case of driven oscillations, the unloaded quality factor can be determined from the Full Width Half Maximum (FWHM), $\Delta\omega_H$

$$Q_0 = \frac{\omega_0}{\Delta\omega_H} \quad (2.2.2)$$

2.2.2 Coupling coefficient

The coupling coefficient is defined as:

$$\kappa = \frac{Z_a}{Z_0} = \frac{R_s}{n^2 Z_0} = \frac{Q_0}{Q_{ext}} \quad (2.2.3)$$

where n is the transformer turn ratio, Q_0 is the unloaded quality factor and Q_{ext} is the external quality factor. If we know the coupling coefficient, the unloaded quality factor can be calculated using:

$$\begin{aligned} \frac{1}{Q} &= \frac{1}{Q_0} + \frac{1}{Q_{ext}} \\ Q_0 &= (1 + \kappa) \cdot Q \end{aligned} \quad (2.2.4)$$

We also get 3 cases for the coupling coefficient, which are:

- $\kappa < 1$: undercritical coupling, $Q > Q_0/2$
- $\kappa = 1$: critical coupling, $Q = Q_0/2$ (no reflection)
- $\kappa > 1$: overcritical coupling, $Q < Q_0/2$

2.2.3 Reflection coefficient

In the conductor, we have an incoming wave (\hat{U}_+, \hat{I}_+) and reflected wave (\hat{U}_-, \hat{I}_-) . Hence we define the complex reflection coefficient as:

$$\rho = \frac{\hat{U}_-}{\hat{U}_+} \quad (2.2.5)$$

The coupling coefficient and the reflection coefficient are related at resonance by:

$$\kappa = \left| \frac{1 + \rho}{1 - \rho} \right| \quad (2.2.6)$$

We shall discuss more about this in the next section.

2.2.4 Shunt impedance

Shunt impedance tells us how much energy is gained by a charged particle when it crosses the cavity. It is defined by:

$$R_s = \frac{U^2}{2P_V} = \frac{1}{P_V} \left| \int_{L/2}^{-L/2} E_0(s) \cdot e^{i\omega_0 s/c} \cdot ds \right|^2 \quad (2.2.7)$$

The impedance of the resonator in fig.2.2.1 is a complex quantity. This value only becomes real at resonance and when it does, it is called the Shunt impedance. This value is typically of the order of $10^6 \Omega$. This is the reason we use a step down transformer in the circuit, using loop coupling, as seen in Eq.(2.2.3).

2.3 Scalar measurement of reflection coefficient

The reflection coefficient we defined in the previous section (eqn. 2.2.5) is a complex value. It looks like:

$$\rho(\Delta\omega) = \rho_0(\Delta\omega) \cdot e^{-2ikl} = \frac{\kappa - (1 + 2iQ_0 \frac{\Delta\omega}{\omega})}{\kappa + (1 + 2iQ_0 \frac{\Delta\omega}{\omega})} \cdot e^{-2ikl}$$

We get this when we investigate only take $\Delta\omega \ll \omega_0$. When this reflection coefficient is measured some distance l away from the cavity, we get the delay factor of e^{-2ikl} .

Now, we can separate the real and imaginary part and get its modulus:

$$|\rho(\Delta\omega)| = |\rho_0(\Delta\omega)| = \sqrt{\frac{(\kappa - 1)^2 + 4Q_0^2 (\Delta\omega/\omega)^2}{(\kappa + 1)^2 + 4Q_0^2 (\Delta\omega/\omega)^2}} \quad (2.3.1)$$

The scalar network analyzer should then look like fig. 2.3.1.

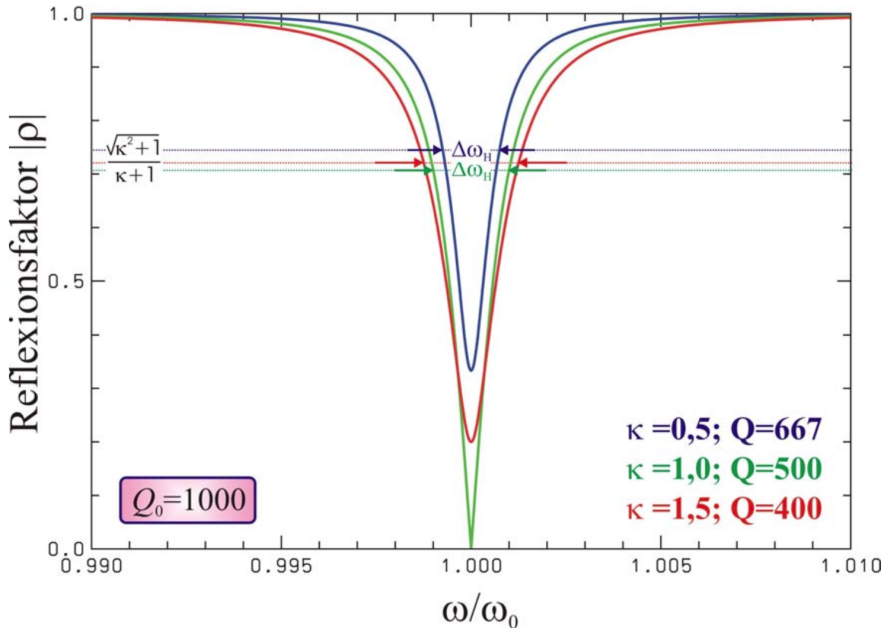


Figure 2.3.1: Reflection coefficient for different values of coupling coefficient and Quality factors along with FWHM ($\Delta\omega_H$). [3]

From the figure, we can see that the reflection is minimum at resonance. At resonance, the value of the reflection coefficient is given by:

$$|\rho(\Delta\omega = 0)| = \left| \frac{\kappa - 1}{\kappa + 1} \right| \quad (2.3.2)$$

The equation can be inverted to calculate the value of coupling coefficient as such:

$$\kappa = \begin{cases} \frac{1+|\rho|}{1-|\rho|} : & \rho > 0 \\ \frac{1-|\rho|}{1+|\rho|} : & \rho < 0 \end{cases} \quad (2.3.3)$$

As such, one cannot distinguish between $\rho > 0$ and $\rho < 0$.

In order to calculate the value of reflection coefficient at FWHM, we use the following relation (which one can derive by using eqn.(2.2.2), (2.2.4) and (2.3.1)):

$$|\rho(\Delta\omega_H/2)| = \frac{\sqrt{\kappa^2 + 1}}{\kappa + 1} \quad (2.3.4)$$

It is important to note that only the case of $\kappa = 1$ do we get the FWHM at $\rho = 1/\sqrt{2}$. This is because of the way we define dB-values, which will be discussed in another section.

In all other cases,

$$|\rho(\Delta\omega_H/2)| = \frac{\sqrt{\kappa^2 + 1}}{\kappa + 1} \neq \frac{1}{\sqrt{2}}$$

The (loaded) quality factor Q is then determined by following Eq. 2.2.2:

$$Q = \frac{\omega_0}{\Delta\omega_H} \quad (2.3.5)$$

The unloaded quality factor can easily be determined from Eq. 2.3.5 above:

$$Q_0 = (1 + \kappa)Q \quad (2.3.6)$$

2.4 Vectorial measurement of reflection coefficient

The vectorial reflection coefficient is given by:

$$\rho(\Delta\omega) = \frac{(\kappa - 1)^2 - 4Q_0^2(\Delta\omega/\omega)^2 - 4i\kappa Q_0 \Delta\omega/\omega}{(\kappa + 1)^2 + 4Q_0^2(\Delta\omega/\omega)^2} \cdot e^{-2ikl} \quad (2.4.1)$$

Neglecting the delay coefficient term, e^{-2ikl} , we get an equation, which when plotted on the complex plane (close to the resonance), ρ_0 describes a circle of radius r around (x_0, y_0) . The radius r is given by:

$$r = \frac{\kappa}{1 + \kappa}$$

We find that all the positions of circles are independent of quality factor and depend only on the coupling coefficient. Another interesting thing we find is that all these circles go through $(-1, 0)$ (as shown in fig. 2.4.1).

Now taking the delay coefficient into account, we see the circles rotate around the origin (fig. 2.4.2). For large values of quality factor, the distortion in the shape of the circle is negligible, but it is quite noticeable in low values of quality factor. We will be neglecting these distortions in our measurements because we such calibrations can be done only on expensive equipments.

In fig. 2.4.2, we also notice that we have an outer circle which is the reflection circle. It represents complete reflection of frequencies far away from the resonance one. The smaller circle is called the resonance circle.

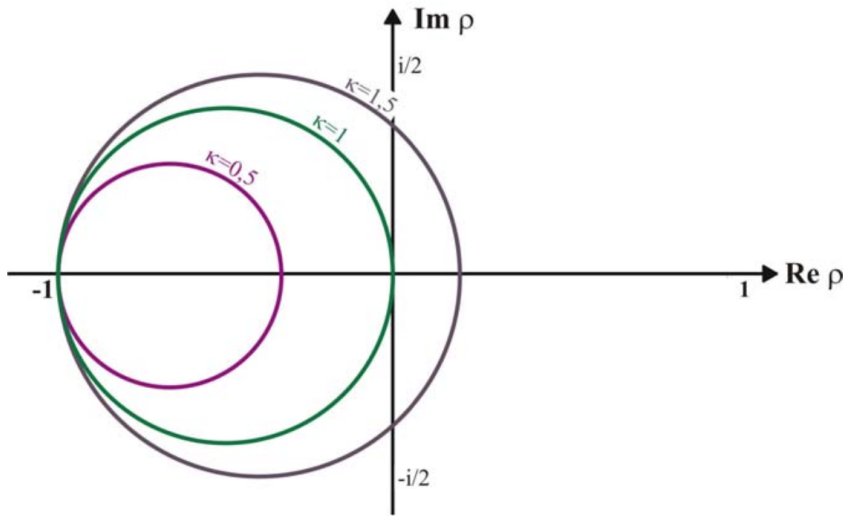


Figure 2.4.1: Different position and radii for different values of κ . [3]

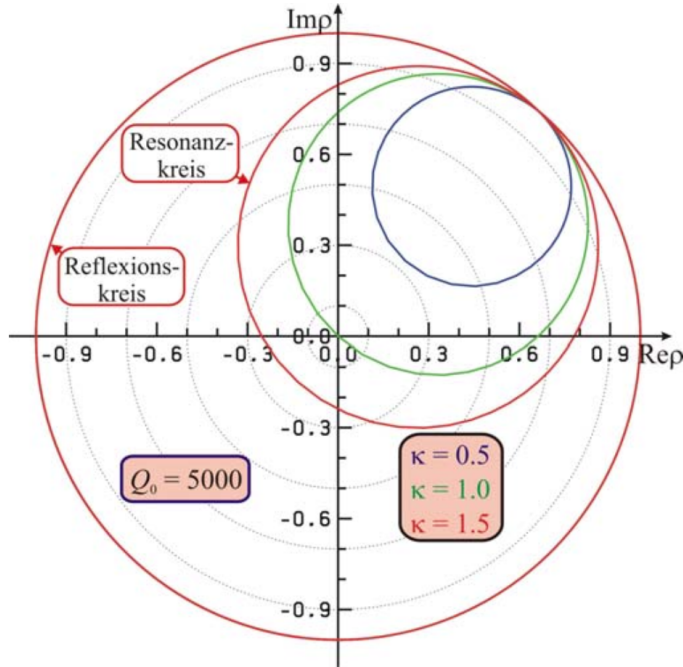


Figure 2.4.2: The delay coefficient rotates the circle around the origin. We can also see the Resonance and Reflection circle. [3]

2.4.1 Determining resonant frequency and coupling

In the Vectorial Network Analyzer (VNA), we see something similar to Fig. 2.4.2. In order to determine the reflection coefficient, we rotate the circles around the origin such that the point of intersection of the resonant circle and reflection circle is on $(-1, 0)$. Since the impedance of the resonator is real at resonance, the curve has to cross the real axis. Therefore, the point at which the resonance circle meets the real axis is the resonance frequency ω_0 .

In order to determine the reflection coefficient, we simply look at the distance between the resonant point and the origin, d , and the radius of the reflection circle, R . The reflection coefficient is then defined as:

$$\rho_0 = d/R$$

The coupling coefficient is given by:

$$\kappa = \frac{1 + \rho_0}{1 - \rho_0}$$

2.4.2 Determining quality factor

Similar to the scalar measurement, we use

$$\frac{\Delta\omega_H/2}{\omega_0} \approx \frac{1 + \kappa}{2Q_0}$$

and we get

$$\rho_0(\pm\Delta\omega_H/2) = -\frac{1}{\kappa+1} \mp i\frac{\kappa}{\kappa+1}$$

Therefore, the frequency shift $\Delta\omega$ from the resonant frequency and hence the FWHM can be determined by the intersection of the resonance circle around $(0, \pm i/2)$. This is essentially the frequency that is $\pi/2$ rotation away from the resonant frequency on the resonance circle.

2.4.3 Determining Power Loss

The power loss in the cavity P can be determined by utilizing the Smith diagram with the reflections circles to determine the standing wave ratio. The standing wave ratio (SWR) quantifies the degree of reflection of a signal. It is ranged from $[1, \infty)$ such that for $\text{SWR} \rightarrow 1$ the signal is totally reflected, and for $\text{SWR} \rightarrow \infty$, the signal is totally transmitted (i.e. no reflections are observed). The SWR can be described as such:

$$S = \frac{|\hat{U}_{max}|}{|\hat{U}_{min}|} = \frac{1 + |\rho|}{1 - |\rho|} \quad (2.4.2)$$

The power dissipation in the resonator can then be described as such:

$$P = \frac{4S}{(1 + S)^2} P_0 \quad (2.4.3)$$

where P_0 is the input power of the signal.

2.5 Bead pull measurement

In order to measure the electric and magnetic field inside the cavity, we cannot use an antenna because that would disturb the field distribution inside. Instead, we introduce a small bead inside the cavity, a small perturbation. This bead, which is usually a dielectric or a conducting object, causes a shift in the resonant frequency, which can be measured. It can also be fixed with a constant excitation with ω_0 and the change in reflection coefficient can be observed. These two things can be used to determine the fields inside the cavity.

2.5.1 Resonant bead pull measurement

The case in which we measure the shift in the resonant frequency is called resonant bead pull measurement. A small teflon bead ($\epsilon_r = 2.1$, $r = 1\text{mm}$) is moved in small increments inside the cavity. For each increment, we get a shift in the resonance frequency $\Delta\omega(z)$. The Electric field, $E_0(z)$ is given by:

$$E_0(z) = \sqrt{2 \cdot \frac{W}{\alpha_s} \cdot \frac{\Delta\omega(z)}{\omega_0}} \quad (2.5.1)$$

where α_s is the perturbing constant:

$$\alpha_S = \frac{1}{2} \cdot (\epsilon - \epsilon_0) \cdot V_S$$

V_S is the volume of the bead.

2.5.2 Non-resonant bead pull measurement

The case in which we measure the change in reflection coefficient without changing the excitation is called non-resonant bead pull measurement. The electric field is determined by:

$$E_0(z) = \sqrt{\frac{(1 + \kappa)^2}{2\kappa Q_0} \cdot \frac{W}{\alpha_S} \cdot |\Delta\rho(z)|} \quad (2.5.2)$$

2.5.3 Shunt impedance

For determining the shunt impedance, it is sufficient to know the electric field. The accelerating voltage U is given by:

$$U = \int_0^L E_0(z) \cdot dz$$

Using this and Eqn. 2.2.7, we can define a delay coefficient as:

$$\Lambda = \left| \frac{\int_{-L/2}^{L/2} E_0(s) \cdot e^{i\frac{\omega_0 s}{c} \cdot ds}}{\int_{-L/2}^{L/2} E_0(s) \cdot ds} \right| = \left| \frac{\int_{-L/2}^{L/2} E_0(s) \cdot \cos\left(\frac{\omega_0 s}{c}\right) \cdot ds}{\int_{-L/2}^{L/2} E_0(s) \cdot ds} \right| \quad (2.5.3)$$

where the time transit factor $e^{i\frac{\omega_0 s}{c}} = \cos\left(\frac{\omega_0 s}{c}\right)$ as we are dealing with real values of frequencies.
And finally, we have for resonant method:

$$R_s = \Lambda \cdot \frac{2Q_0}{\omega_0^2 \cdot \alpha_S} \cdot \left| \int_{-L/2}^{L/2} \sqrt{\Delta\omega(z)} \cdot dz \right|^2 \quad (2.5.4)$$

And for non-resonant method we have:

$$R_s = \Lambda \cdot \frac{(1 + \kappa)^2}{2\omega_0 \kappa \alpha_S} \cdot \left| \int_{-L/2}^{L/2} \sqrt{\Delta\rho(z)} \cdot dz \right|^2 \quad (2.5.5)$$

The energy gain of a particle accelerating within a cavity can then be defined using Eq. 2.2.7, considering that the power dissipation due to the cavity can be related to the measured power $P_v = P/(1 + \kappa)$ as follows:

$$\delta U = \sqrt{\frac{2R_s P}{1 + \kappa}} \quad (2.5.6)$$

This will be used to determine the efficiency of the cavity for particle acceleration.

2.6 dB and DBm

Decibel (symbol: dB), is logarithmic quantity that indicated gain or loss, with respect to a reference value. It is defined as:

$$L_P = 10 \log_{10} \left(\frac{P}{P_0} \right) dB \quad (2.6.1)$$

where P is the measured power and P_0 is the reference power. When we take this reference power $P_0 = 1\text{mW}$, it is known as decibel-milliwatts (dBm). It is defined as:

$$L_P = 10 \log_{10} \left(\frac{P}{1mW} \right) dBm \quad (2.6.2)$$

When talking about root-power quantities (for instance voltage and current), the ratio of the squares is taken.

$$L_F = 10 \log_{10} \left(\frac{F^2}{F_0^2} \right) dB = 20 \log_{10} \left(\frac{F}{F_0} \right) dB \quad (2.6.3)$$

Recalling our discussion from before, about the FWHM, in Eq. 2.3.4, we see that only in the case where $\kappa = 1$ do we get the full 3dB-FWHM, corresponding to the value $\rho = 1/\sqrt{2}$. This is because of how dB is defined in the Eq. 2.6.3.

Chapter 3

Exercise before the experiment

In this pre-lab exercise, we estimate the frequency for various modes of the cavity by using the mode map (Fig. 2.1.1) and using the Eq. 2.1.13. The cylindrical cavity has an inner diameter of 78.5mm and length of 20mm. So we have, $(d/l)^2 = 15.405625$. Therefore, from the mode map, the ten lowest eigenmodes are tabulated in the table 3.1.

Table 3.1: Eigenmodes and their corresponding frequencies calculated using the mode map.

| Eigenmodes | Frequency (GHz) |
|---------------------|-----------------|
| TM_{010} | 2.848 |
| TM_{110} | 4.593 |
| TM_{210} | 6.240 |
| TM_{020} | 6.740 |
| TE_{111} | 7.643 |
| TM_{310} | 7.748 |
| TM_{011} | 7.955 |
| TE_{211} | 8.353 |
| TM_{120} | 8.545 |
| TM_{111}/TE_{011} | 8.733 |

The values calculated using Eq. 2.1.13 is shown in the table 3.2.

Table 3.2: Eigenmodes and their corresponding frequencies calculated using the formula.

| Eigenmodes | Frequency (GHz) |
|---------------------|-----------------|
| TM_{010} | 2.925 |
| TM_{110} | 4.661 |
| TM_{210} | 6.247 |
| TM_{020} | 6.715 |
| TE_{111} | 7.827 |
| TM_{310} | 7.761 |
| TM_{011} | 8.050 |
| TE_{211} | 8.369 |
| TM_{120} | 8.534 |
| TM_{111}/TE_{011} | 8.830 |

Chapter 4

Setup and Procedure

4.1 Experimental Setup

In our experiment, we used three cylindrical cavities, each with a length of $L_{cav} = 20\text{ mm}$ with an inner diameter of $d_{cav} = 78.5\text{ mm}$. The first and second cavity are completely sealed and are free to move, but differ in their coupling position to the radio frequency. The third cavity is open from the sides and is mounted on a rail, in which its position can be freely adjusted and is displayed on an external device digitally. A thread with a teflon bead of radius $r_{bead} = 1\text{ mm}$ and relative permittivity of $\epsilon_{r,bead} = 2.1$ was placed on the same mount such that the bead can pass through the cavity. The cavities used are shown in Fig. 4.1.1.

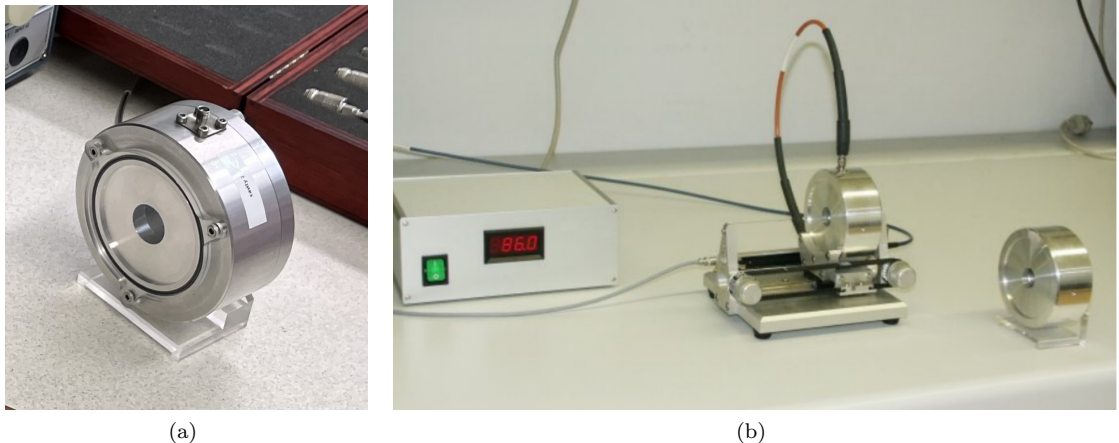


Figure 4.1.1: The three cavities used in this experiment. (a): The cavity with top coupling. The connector that couples the radio frequency can be observed. (b) The cavity with side coupling (right) and the mounted cavity (left) [5]. The detector used to measure the position of the mounted cavity is also shown.

To measure the resonant frequencies, reflection coefficients, and other relevant quantities in our experiment, we utilize a Vector Network Analyzer (VNA) shown in Fig. 4.1.2. The VNA generates a signal from its AC source and it is transmitted through the coaxial cable connected to the ports of the VNA. The resulting transmission or reflection of the signal is then shown on the display as a function of the frequency of the signal (in Hz). The units displayed can be altered between U , the ratio between output and input signal, and $dB = 20 \log_{10}(U)$.

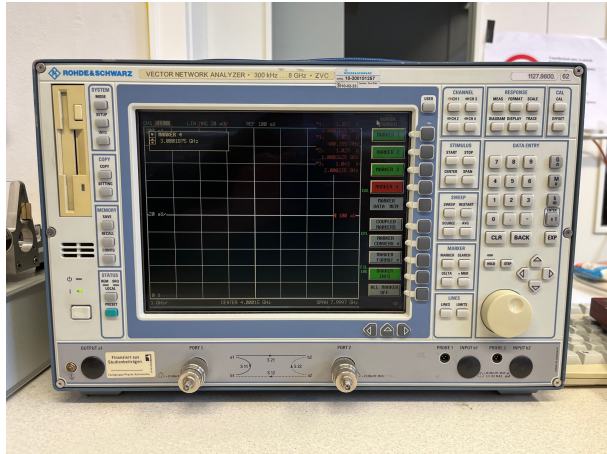


Figure 4.1.2: The Rhode & Schwarz Vector Network Analyzer used in this experiment.

4.2 Procedure

4.2.1 Attenuation and Reflection in Coaxial Cables

As the coaxial cable connects the cavity to the VNA, we need to choose a cable such that it does not interfere with the measurement of the cavity's response. To determine the optimal coaxial cable to use, we thus measured the attenuation and reflection of different coaxial cables at different frequency ranges. In our experiment, this was done for the RG-142 and ST-18 cables with a length of $l_{RG142} = 51.02 \pm 0.10$ cm and $l_{ST18} = 182.55 \pm 0.10$ cm respectively. The uncertainty of the length was obtained from the width of the scale of the measuring apparatus.

To measure the attenuation and reflection, we first calibrated the VNA to the silver RG402 coaxial cable with a length of $l_{RG402} = 30.02 \pm 0.01$ cm. The calibration process was performed using a full-two port calibration with the TOSM algorithm provided by the VNA. The open, short, and load (with termination impedance of 50Ω) at the two ports (port 2 on the VNA and the coaxial cable) were then calibrated by utilizing the provided calibration kit (Fig. 4.2.1).

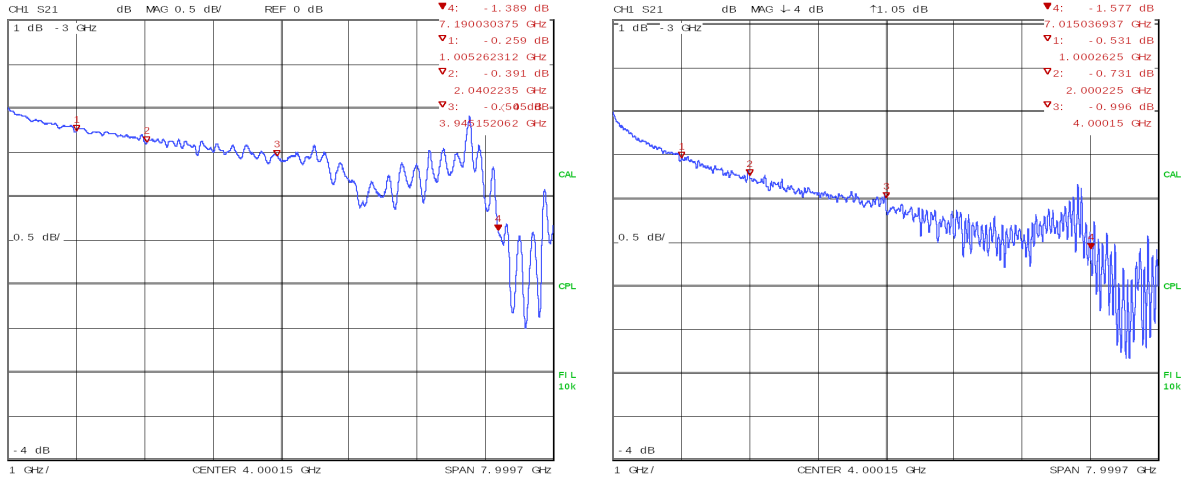


Figure 4.2.1: The open (left), short (middle) and load (right) used for calibration in this experiment.

The attenuation of the signal was then measured by connecting the end of the coaxial cable to the input port (port 2) on the VNA. We then connect the same load from the calibration kit to the end of the coaxial cable to measure the reflection coefficient. Both measurements were performed to verify that the VNA was properly calibrated.

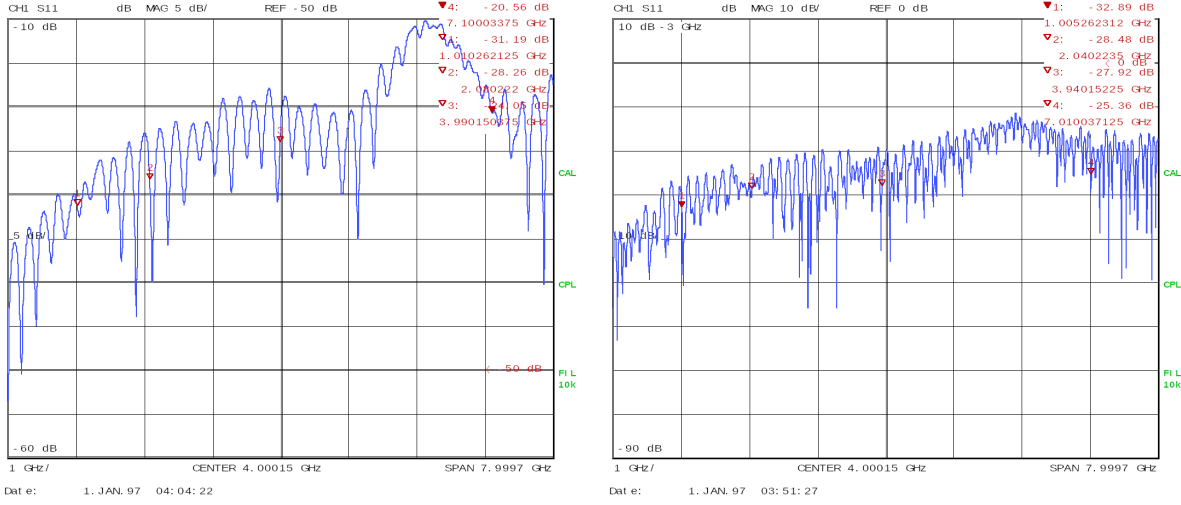
After the calibration was performed with the silver cable, we connected the two coaxial cables to the silver cable and measured their attenuation and reflection coefficient by performing the same procedure as with the silver one. The raw measurements obtained are shown in Fig. 4.2.2. The fluctuations in the signal were taken into account as the uncertainty in the coefficients. We neglected effects due to the connector between the two cables.

The transmission and reflection at several frequencies were then tabulated and were used to determine



(a) Transmission for the RG142 cable.

(b) Transmission for the ST18 cable.



(c) Reflection for the RG142 cable.

(d) Reflection for the ST18 cable.

Figure 4.2.2: The transmission and reflection for the RG142 and ST18 coaxial cables. The values at several frequencies are also shown on the top right of each figure.

the attenuation of the cable. The attenuation λ (in units of dB m^{-1}) of a coaxial cable can be determined by the ratio of the reflected and transmitted power P_R , P_T as such:

$$\lambda = 20 \log_{10} \left(\frac{P_{in}}{P_{out}} \right) = 20 \log_{10} \left(\frac{P_R}{P_T} \right) \quad (4.2.1)$$

The resulting attenuation was then compared to those provided in the datasheets from the manufacturers.

4.2.2 Scalar Measurement

We then connected the brown coaxial cable to the top cavity (cavity with top coupling), and the resulting reflection coefficient was displayed on the VNA. We then pinpointed several points in frequency in which a sharp dip in the reflection curve was observed. Such points corresponded to resonant modes in the cavity. Before taking the measurement of each resonant frequency, the VNA was calibrated using a full one-port procedure, calibration with the kit from Fig. 4.2.1 as before. An example of a resonance in the reflection curve is shown in Fig. 4.2.3. The corresponding reflection coefficient and resonant frequency was then measured. The fluctuations and width of the scales taken into account as uncertainties in the

reflection coefficient. The step size of the VNA was 50 kHz, which was also considered as the uncertainty in frequency measurements.

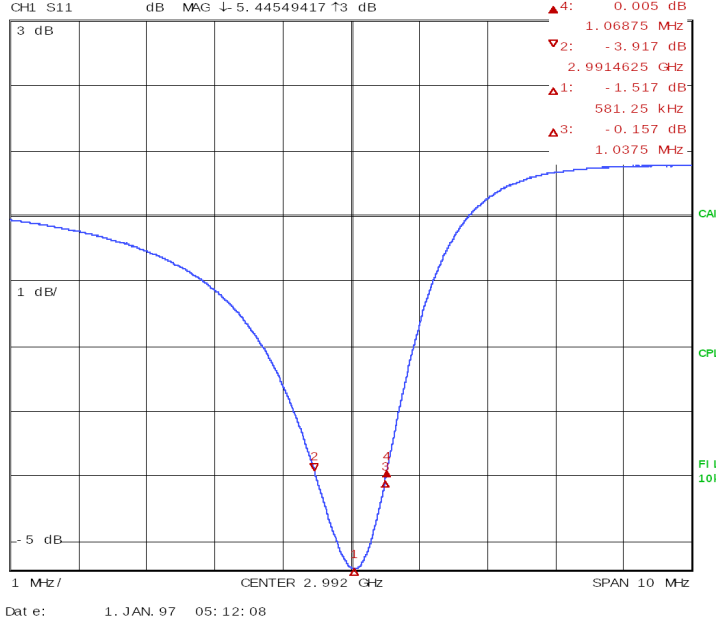


Figure 4.2.3: Reflection curve at a resonant frequency of $\omega_0 = 2.992\ 206\ 875\ \text{GHz}$.

To obtain the full-width half-maximum (FWHM) of the curve, the reflection coefficient obtained at resonance $|\rho(\omega_0)|$ was used to determine the coupling coefficient as shown in Eq. 2.3.3. The reflection coefficient at $\frac{\Delta\omega_H}{2}$ was then evaluated by using Eq. 2.3.4 and the corresponding frequency values, that is, the half of the FWHM, were measured using the display. The loaded and unloaded quality factor was then determined using Eq. 2.3.5 and 2.3.6 respectively. Gaussian error propagation techniques were utilized to obtain the correct uncertainties for relevant quantities.

This procedure was performed for each observed resonance peak until 8 GHz, the maximal frequency in which the VNA can measure. The same analysis was repeated for the side cavity, and the resonant frequency obtained in both cases were compared with the analytical resonant frequencies evaluated from Eq. 2.1.13. The raw data for both cases are presented in Table 4.1 and 4.2.

| ω_0 / GHz | $ \rho(\omega_0) / \text{dB}$ | κ | $ \rho(\Delta\omega_H/2) / \text{dB}$ | $\Delta\omega_H / \text{MHz}$ |
|-------------------------|--------------------------------|----------------------|--|-------------------------------|
| 2.992206875 | -5.445 ± 0.010 | -1.4499 ± 0.0010 | -3.915 ± 0.015 | 2.1375 |
| 4.53973125 | -40.0 ± 5.0 | -1.0513 ± 0.0066 | -28.3 ± 1.0 | 0.575 |
| 6.21559375 | -2.37 ± 0.05 | -2.460 ± 0.053 | -1.819 ± 0.051 | 5.5625 |
| 6.940125 | -9.575 ± 0.50 | -1.233 ± 0.014 | -6.81 ± 0.13 | 5.625 |
| 7.75975 | -4.13 ± 0.080 | -1.639 ± 0.016 | -3.005 ± 0.061 | 8.75 |

Table 4.1: Raw data for relevant quantities measured at resonant modes of top cavity. κ and $|\rho(\Delta\omega_H/2)|$ are calculated quantities used to measure $\Delta\omega_H$.

| ω_0 / GHz | $ \rho(\omega_0) / \text{dB}$ | κ | $ \rho(\Delta\omega_H/2) / \text{dB}$ | $\Delta\omega_H / \text{MHz}$ |
|-------------------------|--------------------------------|----------------------|--|-------------------------------|
| 2.98690625 | -2.404 ± 0.005 | -2.4245 ± 0.0051 | -1.8411 ± 0.0051 | 4.0625 |
| 4.49725 | -1.270 ± 0.020 | -8.41 ± 0.55 | -1.143 ± 0.083 | 1.375 |
| 6.2078875 | -3.755 ± 0.010 | -1.7270 ± 0.0026 | -2.745 ± 0.040 | 0.8125 |
| 7.74540625 | -6.625 ± 0.030 | -1.3556 ± 0.0019 | -4.737 ± 0.070 | 0.875 |

Table 4.2: Same as Fig. 4.1 but for the side cavity.

4.2.3 Vectorial Measurement

We then used the top cavity to determine the resonant frequency and FWHM for the first fundamental eigenmode vectorially. This was done using the reflection curves as shown in Fig. 2.4.2, which is done by switching the display on the VNA to the complex representation.

The resonant frequency was first determined by using the same method as with the scalar analysis. We then switched to the complex representation and rotated the curve such that the point on the curve at resonance intersects with the real axis. The FWHM was then determined by first evaluating for the coupling coefficient, using the same equations as with the scalar analysis. The corresponding values of $|\rho(\frac{\Delta\omega_H}{2})|$ were then determined on the resonant circle, and the resulting frequency values were tabulated. The fluctuations of the measurement were again taken into account as uncertainties in our measurement. We also recorded the input power to be $P_0 = 1.5 \pm 0.1\text{dB}$.

In our measurement, the more accurate method that utilizes the distance between points on the reflection and resonant circle to determine the coupling coefficient was not performed due to the error in the calculated $|\rho(\frac{\Delta\omega_H}{2})|$ when using this method. This may have been resolved if we had used units of power ratios U instead of dB to determine the coupling coefficient. This is also the reason why κ in the scalar measurement yielded negative values. In the future, units in the measurement should be set to U as much as possible.

The obtained values were then used to determine the loaded, unloaded and external quality factor Q , Q_0 , Q_{ext} , as well as the power loss of the cavity. This was first performed without calibrating the VNA, and the same procedure was repeated after calibrating the VNA. The calibration was performed as with the scalar case. The results obtained from both cases were compared and discussed. A raw measurement of the resonant and reflection curves in both uncalibrated and calibrated cases are shown in Fig. 4.2.4.

4.2.4 Bead-Pull Measurement

We then connected the coaxial cable to the cavity mounted on the rail. Using the same method as with the scalar case, the location of the fundamental resonant mode was determined and the resonant frequency and FWHM was tabulated. These values were used to evaluate the quality factor Q , stored energy W , and the power loss of the cavity.

The cavity was then positioned such that the teflon bead was outside of the cavity. The position of the cavity was then adjusted, and using the scalar representation the change in resonant frequency $\Delta\omega_0$ and change in reflection coefficient at resonant frequency $|\Delta\rho(\omega_0)|$ were tabulated. The fluctuations and stepsize of the measurements were taken into account as the uncertainties in measurement. This was performed until the bead was completely outside of the cavity, which corresponds to a length of approximately 40 mm. The raw data can be observed in the Appendix section.

Using Eq. 2.5.1 and 2.5.2, the unperturbed electric field strength $E_0(z)$ was then determined for each position of the bead. Using the power loss obtained from above, we then evaluated the shunt impedance R_s as defined by Eq. 2.5.4 and 2.5.5 by utilizing cubic interpolations and Gauss-Legendre quadrature integration techniques. The transit time factor $\cos(\frac{\omega_0 z}{c})$ was also taken into account when evaluating the shunt impedance, and the electric fields when considering such time factor was compared to those without this factor.

Finally, the energy gain of an accelerating particle δU was determined for several input powers using Eq. 2.5.6. This was used to observe if our cavity was suited for particle accelerator experiments.

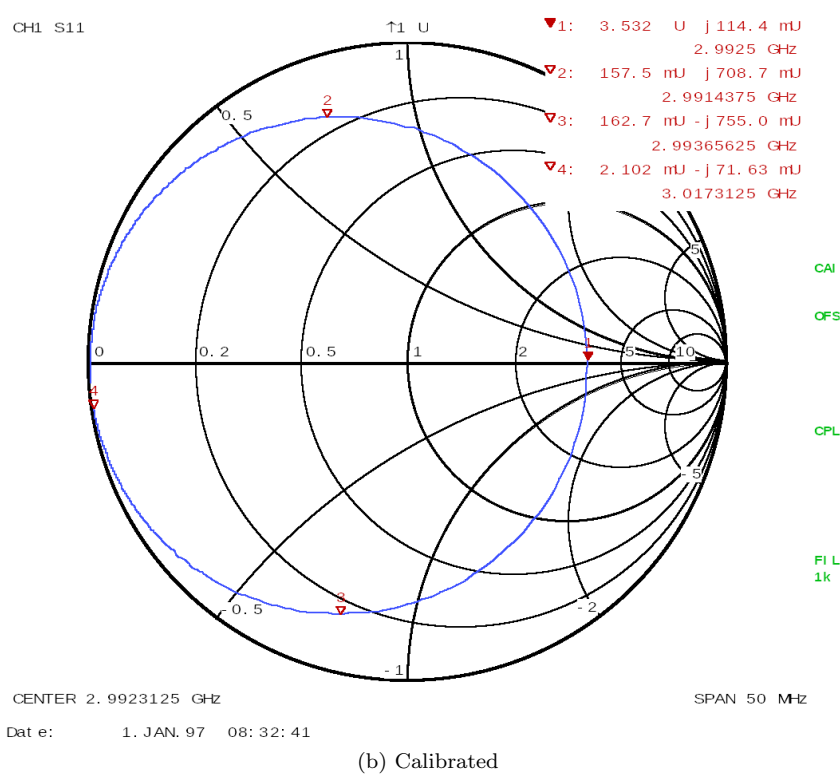
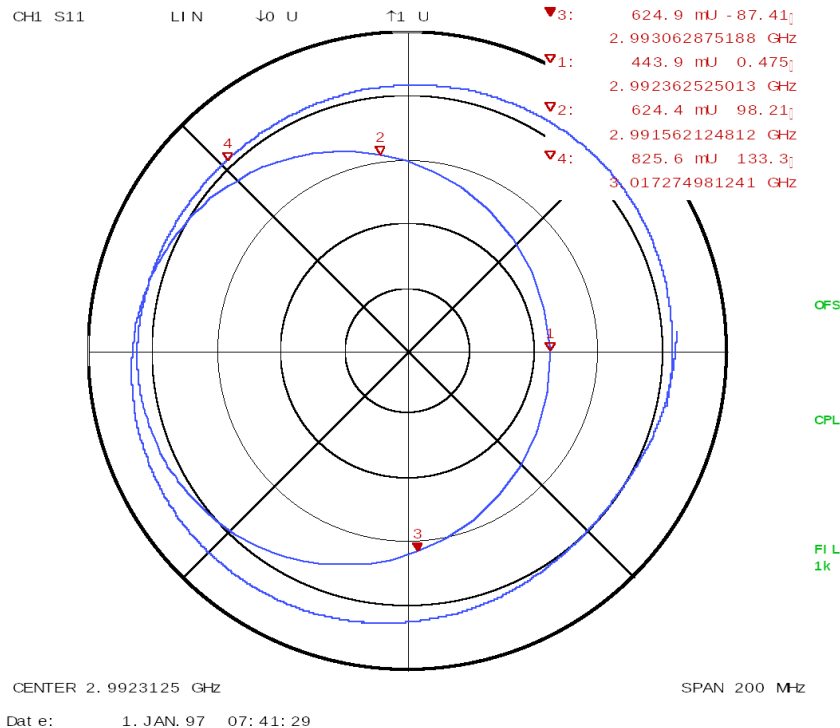


Figure 4.2.4: Vectorial measurement of the fundamental resonant mode (a) without and (b) with calibration. The curves are represented in linear polar and Smith representation respectively. The resonant frequency and points at half of the FWHM are indicated with markers 1, 2, 3 respectively.

Chapter 5

Results and Discussion

5.1 Attenuation of Coaxial Cables

Fig. 5.1.1 shows the attenuation of the RG142 and ST18 cables for frequency values at approximately 1, 2, 4, and 7 GHz. The attenuations as given by the datasheets of the corresponding cable from the manufacturers are also shown [6], [7]. To match the amplitudes from our measurement with those from the datasheet, we had to apply a normalization factor of $N = 1 \times 10^{10}$ and 1×10^2 for the RG142 and ST18 cables respectively. From the comparisons between the two attenuations, it is clear that the ST18 cable induces less power losses, even at higher frequencies. This implies that we should be using the ST18 cable for our measurement to prevent the signal loss in the coaxial cable to influence our measurements.

In our experiment, however, we have chosen to use the RG142 cable. This, as can be seen by Fig. 5.1.1, will influence the reflection measurements at higher frequencies. This may have been a main cause in the larger uncertainty in measurement of higher resonant modes. In the future, the ST18 cable should be used instead of the RG142 cable.

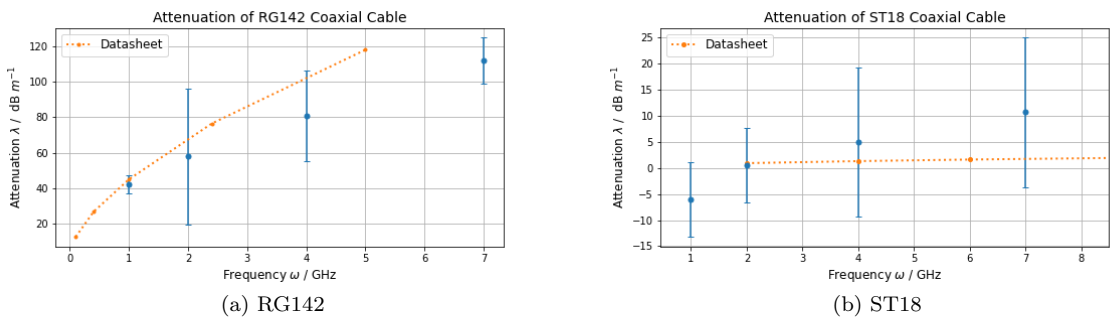


Figure 5.1.1: The attenuation of the (a) RG142 and (b) ST18 cable.

5.2 Scalar Measurement

Tables 5.1 and 5.2 show the relevant parameters associated to each resonant mode in the cavity, i.e. the coupling coefficient κ , the FWHM $\Delta\omega_H$, the loaded and unloaded quality factor (Q , Q_0 respectively). The residual with the theoretical resonant frequency (table 3.2) is also shown below. This is shown for the top and side cavity respectively.

From our results, we observe that the resonant frequencies obtained are close to the theoretical values that we have computed analytically with a deviation of approximately ~ 0.05 GHz for both cases. We observe that for all values of the coupling coefficient, they attain negative values, which is due to the fact that we have used dB as our unit of the reflection coefficient when calculating for κ using Eq. 2.3.3. This, however, had no notable effect on the measurement of the FWHM, as we attain reasonable values of the FWHM for both cases.

When observing the loaded and unloaded quality factor, we see that values vary around $10^2 \sim 10^3$. In general, we observe that $Q > Q_0/2$, which implies that most of the oscillatory modes that we obtain

are undercritically coupled. The resonant mode with $\omega_0 = 4.49725$ GHz, however, shown overcritical coupling instead, which yields a larger deviation from the theoretical resonant frequency. We also observe that as $Q \approx Q_0/2$, we obtain more accurate measurements of the resonant frequency.

| ω_0/GHz | κ | $\Delta\omega_H/\text{MHz}$ | $Q(\times 10^3)$ | $Q_0(\times 10^3)$ | $ \omega_0 - \omega_{thr} /\text{GHz}$ |
|-----------------------|----------------------|-----------------------------|---------------------|---------------------|--|
| 2.992206875 | -1.4499 ± 0.0010 | 2.1375 | 1.3999 ± 0.0093 | 0.6298 ± 0.0044 | 0.0668 |
| 4.53973125 | -1.0513 ± 0.0066 | 0.5750 | 7.90 ± 0.19 | 0.405 ± 0.0053 | 0.1214 |
| 6.21559375 | -2.460 ± 0.053 | 5.5625 | 1.1174 ± 0.0028 | 1.631 ± 0.060 | 0.0317 |
| 6.940125 | -1.233 ± 0.014 | 5.6250 | 1.2338 ± 0.0031 | 0.288 ± 0.017 | 0.2251 |
| 7.75975 | -1.639 ± 0.016 | 8.750 | 0.8868 ± 0.0014 | 0.556 ± 0.014 | 0.00153 |

Table 5.1: Calculated quantities for resonant modes for the top cavity. The residual with the analytical resonant frequency is also shown.

| ω_0/GHz | κ | $\Delta\omega_H/\text{MHz}$ | $Q(\times 10^3)$ | $Q_0(\times 10^3)$ | $ \omega_0 - \omega_{thr} /\text{GHz}$ |
|-----------------------|----------------------|-----------------------------|---------------------|---------------------|--|
| 2.98690625 | -2.4245 ± 0.0051 | 4.0625 | 0.7352 ± 0.0026 | 1.0473 ± 0.0052 | 0.0615 |
| 4.49725 | -8.41 ± 0.55 | 1.375 | 3.270 ± 0.034 | 242 ± 18 | 0.1640 |
| 6.2078875 | -1.7270 ± 0.0026 | 0.8125 | 7.64 ± 0.13 | 5.555 ± 0.099 | 0.0394 |
| 7.74540625 | -1.3556 ± 0.0019 | 0.875 | 8.85 ± 0.14 | 3.147 ± 0.054 | 0.0158 |

Table 5.2: Same as Table 5.1 but for the side cavity.

We now compare between the results of the top and side cavity. We first notice that while we were able to observe 5 resonant modes in the top cavity, only 4 such modes were observed in the side cavity. This may be caused by the longitudinal-dependence of the missing resonant mode (corresponding to the TM_{020}), as the side coupling may have affected the signal going through the cavity. Fig. 5.2.1 shows the difference between the resonant frequencies obtain from the top and side cavity. From this, we observe that deviations are on order 10^{-2} , yielding similar results between the two couplings. We further observe that for the resonant mode at $\omega \approx 4.49$ GHz, the deviation is the largest. This may be caused by the overcritical coupling observed from the side cavity at this resonant frequency as mentioned previously.

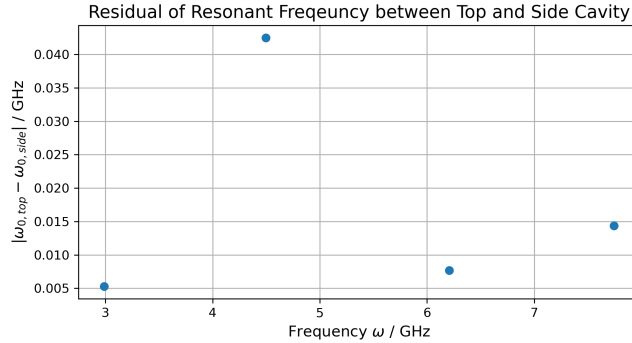


Figure 5.2.1: Residual between the resonance frequencies of the top and side cavity.

5.3 Vectorial Measurement

Table 5.3 shows the measured and calculated quantities obtained from the vectorial measurement at the fundamental resonant mode. This is shown both for the uncalibrated and calibrated measurements. Between the two measurements, we observe that the quality factor from the calibrated results is much larger, indicating a better measurement after calibration. The power lost between the two measurements do not differ, implying that the calibration does not largely affect the power lost in the system.

Comparing our obtained data to those from the scalar measurement in Table 5.1, we observe that the quality factor obtained is much larger, and the value of κ is more closer to unity, indicating that with this measurement, the accuracy of the experiment increases. This is also observed by the standing wave

| | Uncalibrated | Calibrated |
|-------------------------------|----------------------------|----------------------------|
| ω_0 / GHz | 2.992362525013 | 2.9915625 |
| κ | -1.0045157 ± 0.0000051 | -1.0049865 ± 0.0000030 |
| $\Delta\omega_H / \text{MHz}$ | 3.001 | 2.219 |
| Q_0 | 1998.407 ± 0.012 | 3368.1 ± 2.1 |
| Q_{ext} | 1989.435 ± 0.015 | 2248.3 ± 1.4 |
| SWR S | 1.0045157 ± 0.0000051 | 1.003447 ± 0.0000030 |
| P / mW | 1.567 ± 0.023 | 1.567 ± 0.023 |

Table 5.3: Calculated quantities from uncalibrated and calibrated vectorial measurement.

ratio, as its value is close to unity. This tells us that the vectorial method yields a more accurate and stable result.

5.4 Bead-Pull Measurement

From the bead-pull measurement, we first determined the relevant quantities at the fundamental resonant mode, corresponding to the TEM_{010} mode. Table 5.4 shows the parameters obtained from our measurement with an input power of $P_0 = 1.189 \pm 0.01151 \text{ mW}$. All values were calculated as with the previous section, and the stored energy $W = Q_0 P / \omega_0$.

| ω_0 / GHz | κ | $\Delta\omega_H / \text{MHz}$ | Q | P / mW | W / nJ |
|-------------------------|-------------------------|-------------------------------|---------------|---------------------|-------------------|
| 2.9939375 | 1.197230 ± 0.000058 | 0.712 | 4205 ± 42 | 1.1789 ± 0.0114 | 3.638 ± 0.050 |

Table 5.4: Calculated quantities for scalar measurement with the mounted cavity, used for the bead-pull measurement.

We then evaluated for the electric field E_0 using both resonant and non-resonant methods. Fig. 5.4.1 shows the electric field as a function of the position of the bead z with and without including the time transit factor $\cos(\omega_0 z / c)$.

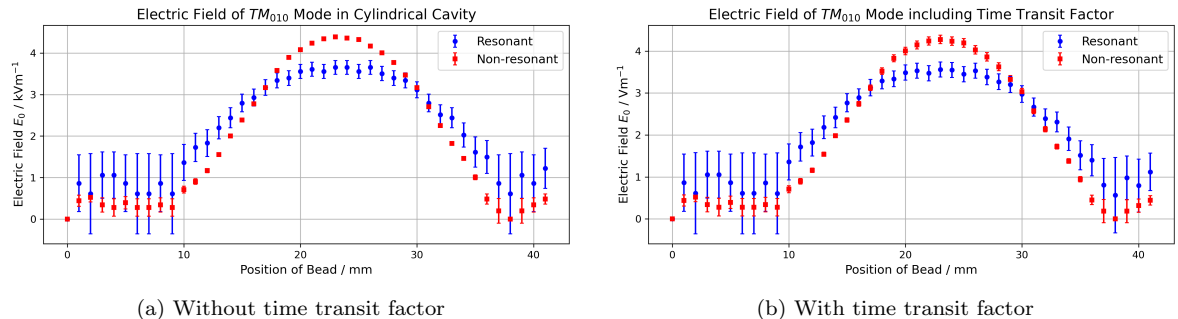


Figure 5.4.1: The electric field E_0 for different positions of the bead z (a) not including and (b) including the time transit factor. The results from both resonant and non-resonant method are shown.

We observe that while both behaviours yield similar oscillatory behaviours, the results from the resonant method have a flatter curve with a lower maximal amplitude of $3.65 \pm 0.16 \text{ kV m}^{-1}$ compared to the non-resonant method, which has a maximal amplitude of $4.390 \pm 0.040 \text{ kV m}^{-1}$. Furthermore, the uncertainty of the results from the resonant method also have larger uncertainties compared to the non-resonant method. As both measurements should ideally yield the same result, such difference between the two methods may have been caused by imperfect calibrations before measurement. When we include the time transit factor, we observe that the amplitude of the electric field decreases, yielding a maximal amplitude of $3.56 \pm 0.18 \text{ kV m}^{-1}$ and $4.27 \pm 0.10 \text{ kV m}^{-1}$ for the resonant and non-resonant method respectively. The overall structure, however, does not differ with the inclusion of this factor.

We now evaluate the shunt impedance using the obtained electric field and the corresponding parameters determined from Table 5.3. This was performed for the results obtained from both the resonant and

non-resonant method using Eq. 2.5.5 and 2.5.4. After performing integration, we obtain the following for the shunt impedance:

$$R_{s,res} = 3.316 \pm 0.032 \text{ M}\Omega$$

$$R_{s,non-res} = 3.791 \pm 0.037 \text{ M}\Omega$$

Using the shunt impedance we obtained for our cavity, we can determine if our cavity is sufficient to accelerate particles. To do this, we first calculate the energy gain of a particle (here, an electron) after passing through our cavity with different input powers. Table 5.5 show the energy gain using the shunt impedance evaluated from both resonant and non-resonant methods for different input radiofrequency powers P_0 .

| P_0 / kW | $\delta U_{res} / \text{keV}$ | $\delta U_{non-res} / \text{keV}$ |
|-------------------|-------------------------------|-----------------------------------|
| 1 | 56.52 ± 0.27 | 60.43 ± 0.29 |
| 10 | 178.72 ± 0.86 | 191.10 ± 0.93 |
| 100 | 565.2 ± 2.7 | 604.3 ± 2.9 |
| 1000 | 1787.2 ± 8.7 | 1910.1 ± 9.3 |

Table 5.5: Energy gain of electron under cavity used in this experiment for several input radiofrequency powers.

We observe that for an input power of 100 kW, we obtain an energy gain on the order of 100 keV, which is a factor of 10 lower than typical values for acceleration energies for particles with this input power. This shows that our cavity is not suitable to accelerate particles.

Chapter 6

Conclusion and Outlook

6.1 Conclusion

In our experiment, we observed if a given cavity was suitable for particle acceleration. To this end, we had to first determine the reflection coefficient of the signal transmitted through the coaxial cable at different resonant modes of the cavity. This would yield reflection curves that dip sharply to $|\rho| \approx 0$ near resonance of the cavity. In order to determine the most efficient coaxial cable to use (i.e. that with the least power loss), the attenuation of the coaxial cable was measured. While we observed that the ST18 coaxial cable yield lower attenuation, we used the RG142 cable instead. In future experiments, the attenuation of the cable should be carefully considered before performing the rest of the measurements.

The resonant frequencies at dips in the reflection curve was measured using a Vector Network Analyzer (VNA), and from this the coupling coefficient κ and $|\rho(\Delta\omega_H/2)|$ was computed. The FWHM of the curve was then measured from such values. The quality factor Q , which quantifies the degree of damping in the system, was then computed. In our analysis, we compared the behaviour between

avities which differed in their location of coupling which yielded deviations of order 10^{-2} . Deviations between the analytical resonant frequencies were also as large as 10^{-2} , which indicate that our results are in good agreement with expected values. The relationship between the quality factor and the comparison with theoretical values were also observed.

The results from the scalar measurement was also compared from those obtained by measuring the corresponding values in a vectorial representation. In this way, the corresponding quantities are much easier to obtain as the coupling coefficient, resonant frequency, and FWHM can be determined pictorially using a Smith diagram. We, however, used the same scalar method to measure the resonant frequency and observed the corresponding data in a vectorial representation. In future experiments, proper measurements in this format should be performed.

To directly quantify the performance of acceleration for charged particles, we performed a bead-pull measurement where the perturbation of the resonant frequency and $|\rho(\omega_0)$ was measured due to a bead passing through the cavity. The electric field within the cavity was computed using two different methods which showed similar structures with different maximal amplitudes. After taking into account of the time transit factor, the shunt impedance was evaluated, yielding $R_{s,res} = 3.316 \pm 0.032 \text{ M}\Omega$ and $R_{s,non-res} = 3.791 \pm 0.037 \text{ M}\Omega$ for the resonant and non-resonant method respectively. These impedances were used to quantify the energy gain of an electron in our cavity at different input powers. This did not yield sufficient acceleration voltages for the electron, implying that our cavity is not suited for particle acceleration.

6.2 Outlook

This experiment consisted of a lot of small details that needed to be taken into account. Due to the time constraints, it is vital to be able to operate the VNA smoothly. This will yield less uncertainty and confusion when performing measurements. Furthermore, each step should be carefully verified and comprehended (as with the attenuation of the coaxial cable) before moving to the next step, as small misconceptions may allow measurements that are not as accurate as one could have done. To extend such an experiment, one can observe the resonant frequencies for different cavity geometries. This can also be done by considering cavities with different materials, ex copper vs iron.

Chapter 7

Appendix

In this section, we will provide with supplementary data that is not within the scope of the main report, but can nevertheless be useful to observe.

| z / mm | $\Delta\omega_0$ / kHz | $ \Delta\rho $ / dB |
|----------|------------------------|---------------------|
| 41.1 | 0 | 0 |
| 42.1 | 6.25 | 0.005 |
| 43.1 | 3.125 | 0.007 |
| 44.1 | 9.375 | 0.003 |
| 45.1 | 9.375 | 0.002 |
| 46.1 | 6.25 | 0.004 |
| 47.1 | 3.125 | 0.002 |
| 48.1 | 3.125 | 0.002 |
| 49.1 | 6.25 | 0.003 |
| 50.1 | 3.125 | 0.002 |
| 51.1 | 15.625 | 0.013 |
| 52.1 | 25 | 0.021 |
| 53.1 | 28.125 | 0.035 |
| 54.1 | 40.625 | 0.062 |
| 55.1 | 50 | 0.103 |
| 56.1 | 65.625 | 0.146 |
| 57.1 | 71.875 | 0.198 |
| 58.1 | 84.375 | 0.258 |
| 59.1 | 93.75 | 0.329 |
| 60.1 | 96.875 | 0.390 |
| 61.1 | 106.2 | 0.428 |
| 62.1 | 109.37 | 0.461 |
| 63.1 | 106.2 | 0.484 |
| 64.1 | 112 | 0.495 |
| 65.1 | 112 | 0.488 |
| 66.1 | 106.2 | 0.481 |
| 67.1 | 112 | 0.446 |
| 68.1 | 103.12 | 0.412 |
| 69.1 | 96.875 | 0.365 |
| 70.1 | 93.75 | 0.309 |
| 71.1 | 81.25 | 0.258 |
| 72.1 | 65.625 | 0.188 |
| 73.1 | 53.125 | 0.130 |
| 74.1 | 50 | 0.085 |
| 75.1 | 34.375 | 0.055 |
| 76.1 | 21.875 | 0.026 |
| 77.1 | 18.75 | 0.006 |
| 78.1 | 6.25 | 0.001 |
| 79.1 | 3.125 | 0 |
| 80.1 | 9.375 | 0.001 |
| 81.1 | 6.25 | 0.003 |
| 82.1 | 12.5 | 0.006 |

Table 7.1: $\Delta\omega_0$ and $|\Delta\rho|$ from the bead-pull measurement at different positions of the bead.

Bibliography

- [1] W. C. Chew, *Lecture notes on ece 604 electromagnetic field theory*, Fall 2020.
- [2] W. Hillert, *Accelerator physics 1*, Summer 2006.
- [3] ——, *E106 hohlraumresonatoren / cavities: Details on the experimental method*. [Online]. Available: <http://www-elsa.physik.uni-bonn.de/Lehrveranstaltungen/FP-E106/E106-Details.pdf>.
- [4] D. J. Griffiths, “Electromagnetic waves,” in *Introduction to electrodynamics*; 3rd ed. Upper Saddle River, NJ: Prentice-Hall, 1999, ch. 9.
- [5] M. Switka, *E106 cavities assignments and details of procedure and analysis*, Mar. 2022.
- [6] *St18/smam/smam/12*, Verical - An arrow company. [Online]. Available: <https://www.verical.com/datasheet/huber-suhner-cable-assembly-st18-smam-smam-12-698033.pdf>.
- [7] *Rg142 datasheet*, REV 1.0, Fairview Microwave, 2018. [Online]. Available: <https://www.fairviewmicrowave.com/images/productPDF/RG142.pdf>.